AGU PUBLICATIONS

JGR

Journal of Geophysical Research: Atmospheres

AUTHOR'S PREFACE TO A SPECIAL COLLECTION

10.1002/2013JD020484

Special Section:
Suomi NPP Calibration and Validation Scientific Results

This article is a companion to *Flynn et al.* [2014] doi:10.1002/2013JD020467 and *Seftor et al.* doi:10.1002/2013JD020472.

Correspondence to:
X. Wu,
Xiangqian.Wu@noaa.gov

Citation:
Wu, X., et al. (2014), Evaluation of the Sensor Data Record from the nadir instruments of the Ozone Mapping Profiler Suite (OMPS), *J. Geophys. Res. Atmos.*, *119*, 6170–6180, doi:10.1002/2013JD020484.

Received 18 JUL 2013
Accepted 7 FEB 2014
Accepted article online 17 FEB 2014
Published online 20 MAY 2014

Evaluation of the Sensor Data Record from the nadir instruments of the Ozone Mapping Profiler Suite (OMPS)

Xiangqian Wu[1], Quanhua Liu[2], Jian Zeng[3], Michael Grotenhuis[3], Haifeng Qian[4], Maria Caponi[5], Larry Flynn[1], Glen Jaross[6], Bhaswar Sen[7], Richard H. Buss Jr.[8], William Johnsen[9], Scott Janz[6], Chunhui Pan[2], Jianguo Niu[10], Trevor Beck[1], Eric Beach[4], Wei Yu[4], M. K. Rama Varma Raja[11], Derek Stuhmer[12], Daniel Cumpton[9], Cristina Owen[12], and Wen-Hao Li[7]

[1]Center for Satellite Applications and Research, NOAA/NESDIS, College Park, Maryland, USA, [2]Cooperative Institute for Climate and Satellites, University of Maryland, College Park, Maryland, USA, [3]ERT, Inc. @ Center for Satellite Applications and Research, NOAA/NESDIS, College Park, Maryland, USA, [4]IMSG, Inc. @ Center for Satellite Applications and Research, NOAA/NESDIS, College Park, Maryland, USA, [5]SEAMM_s Caponi and Associates, Manhattan Beach, California, USA, [6]NASA/GSFC, Greenbelt, Maryland, USA, [7]Northrop Grumman Aerospace Systems, Redondo Beach, California, USA, [8]Innovim, Lanham, Maryland, USA, [9]Raytheon Intelligence, Information and Services, Raytheon Company, Aurora, Colorado, USA, [10]System Research Group (SRG) @ Center for Satellite Applications and Research, NOAA/NESDIS, College Park, Maryland, USA, [11]Science Systems and Applications, Inc., Lanham, Maryland, USA, [12]Raytheon Intelligence, Information and Services, Omaha, Nebraska, USA

Abstract This paper evaluates the first 15 months of the Ozone Mapping and Profiler Suite (OMPS) Sensor Data Record (SDR) acquired by the nadir sensors and processed by the National Oceanic and Atmospheric Administration Interface Data Processing Segment. The evaluation consists of an inter-comparison with a similar satellite instrument, an analysis using a radiative transfer model, and an assessment of product stability. This is in addition to the evaluation of sensor calibration and the Environment Data Record product that are also reported in this Special Issue. All these are parts of synergetic effort to provide comprehensive assessment at every level of the products to ensure its quality. It is found that the OMPS nadir SDR quality is satisfactory for the current Provisional maturity. Methods used in the evaluation are being further refined, developed, and expanded, in collaboration with international community through the Global Space-based Inter-Calibration System, to support the upcoming long-term monitoring.

1. Introduction

The Ozone Mapping and Profiler Suite (OMPS) is a new generation of space-based sensor suite that provides daily measurements of global three-dimensional distribution of atmospheric ozone and other constituents [*Flynn et al.*, 2006]. It is one of the five instruments for the Joint Polar Satellite System (JPSS). The first spacecraft of JPSS, the Suomi National Polar-orbiting Partnership (S-NPP) satellite, was launched on 28 October 2011. The OMPS on S-NPP consists of three instruments that operate synergistically. The Nadir Mapper (NM) acquires each day a global map of total column (TC) ozone in the atmosphere. The Nadir Profiler (NP) measures ozone profile near the nadir. In addition to these nadir-viewing instruments, the OMPS on S-NPP carries an experimental limb-viewing instrument, the Limb Profiler [LP, *Jaross et al.*, 2014], which retrieves ozone profile at higher vertical resolution than the NP. With these three instruments, OMPS extends into future the long-term ozone monitoring by Total Ozone Mapping Spectrometer [TOMS, *McPeters et al.*, 1996], Ozone Monitoring Instrument [OMI, *Levelt et al.*, 2006], Solar Backscatter Ultraviolet Radiometer [SBUV/2, *Hilsenrath et al.*, 1995], SCanning Imaging Absorption spectroMeter for Atmospheric CHartographY [SCIAMACHY, *Gottwald et al.*, 2006], and the Global Ozone Monitoring Experiment-2 [GOME-2, *Klaes et al.*, 2007]. Details about the OMPS, other instruments, and the JPSS program are described elsewhere in this Special Issue.

OMPS was built by the Ball Aerospace and Technologies Corporation (BATC) to government specifications that incorporate inputs from ozone science community. The instruments were thoroughly characterized and calibrated prior to launch. Before and shortly after OMPS opened its door in January 2012, the OMPS team conducted Early Orbit Checkout (EOC) that demonstrated the successful transition of instrument calibration

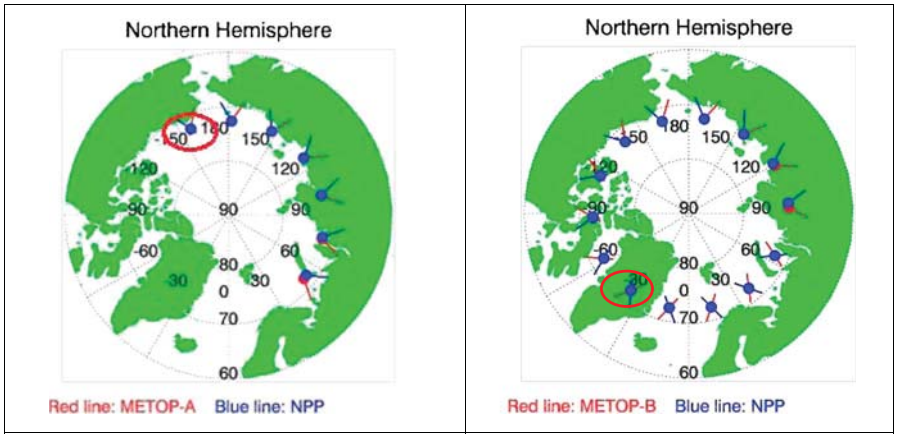

Figure 1. Simultaneous Nadir Overpass (SNO) events between Ozone Mapping and Profiler Suite (OMPS) on Suomi National Polar-orbiting Partnership (S-NPP) and GOME-2 on (left) METOP-A (25 March 2013) and (right) METOP-B (2 March 2013) over the Arctic region. There can be many SNO events in 1 day and, typically, in a few days consecutively for about every 50 days; only one each for METOP-A/B marked in red were analyzed in detail. SNO events also occur in Antarctica, but they often occur in day light over one of the polar regions. Figure courtesy of NOAA Calibration Center.

from pre-launch to on-orbit. During the ensuing period of Intensive Calibration and Validation (ICV), the baseline solar irradiance and wavelength were established and the weekly update of dark current was implemented. Initial evaluations [*Pan et al*., 2013] indicated that OMPS performance has been consistent with the pre-launch instrument characterization and met the expectation. Currently, the OMPS products are at the Provisional maturity, in transition to the Validated maturity in early 2014 when Long-Term Monitoring (LTM) will become the focus of post-launch activities.

Data collected by the OMPS instrument are processed by the Interface Data Processing Segment [IDPS, *Rodriguez et al*., 2003] at the National Oceanic and Atmospheric Administration (NOAA) into higher level products that include the Raw Data Records (RDR), Sensor Data Records (SDR), and Environmental Data Records (EDR). This paper provides a preliminary evaluation of the OMPS SDR using the first 15 months of the IDPS data, including an inter-comparison with a similar satellite instrument in section 2, an evaluation using a radiative transfer model in section 3, and an assessment of stability in section 4. While not meant to be a thorough validation, this evaluation gives an initial assessment of the overall data quality, in particular whether any gross errors or unexpected characteristics exist in the data products. All evaluations are limited to the nadir sensors, as limb sensor SDR are not generated at IDPS. Additional evaluations of OMPS EDR products have been provided in a companion paper by *Flynn et al*. [2014].

2. Comparison With GOME-2

The GOME-2 measures radiances in a spectral range (240–790 nm) that includes the spectral coverage of NP (250–310 nm), and NM (300–380 nm). It was first launched onboard the METOP-A satellite in October 2006 and, more recently, onboard the METOP-B satellite in September 2012. GOME-2 data have been validated and available since February 2007 for GOME-2/METOP-A and since May 2013 for GOME-2/METOP-B, both in near-real time and in operational status with processor version 5 [*Munro et al*., 2008; *Lang*, 2012]. Because of the orbit characteristics of METOP-A/B and S-NPP, their ground tracks cross each other about every 50 days at approximately the same time over certain locations in polar regions, for which the two satellites are said to have "Simultaneous Nadir Overpass" [SNO, *Cao et al*., 2004]. These SNO events are good opportunities to compare similar sensors on the two satellites. Figure 1 depicts several SNO events in 1 day, including the two (marked in circles) at 2152 UTC on 25 March 2013 for METOP-A (left panel) and at 1256 UTC on 2 March 2013 for METOP-B (right panel). These two events, for which the differences in time and space of the nadir measurements were minimal (by 43 s and 3.11 km between METOP-A and S-NPP with a solar zenith angle of 70.32°, and by 20 s and 1.56 km between METOP-B and S-NPP with a solar zenith angle of 79.45°), will be examined in some detail. SNO events also occur over the Antarctica; they were not used because the solar zenith angle was larger than 90° on those days.

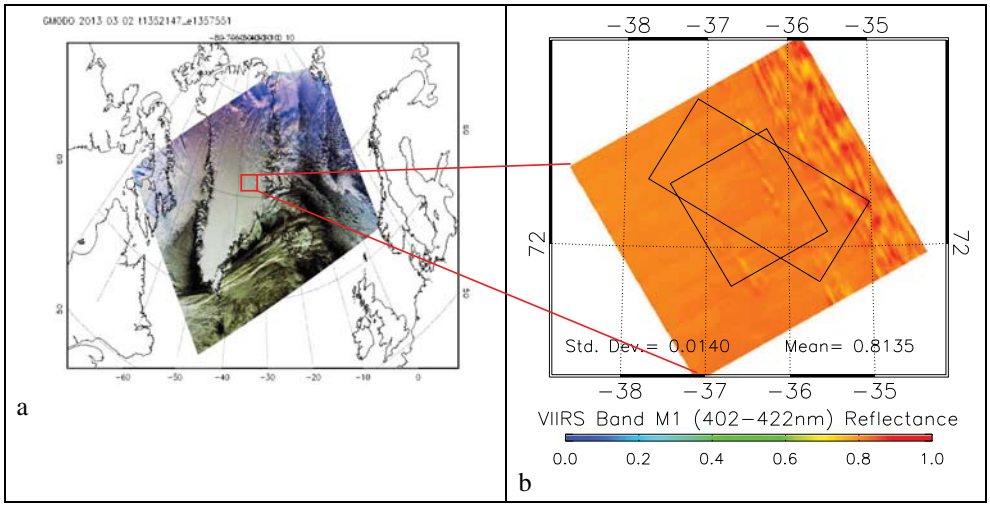

Figure 2. True color image by Visible Infrared Imaging Radiometer Suite (VIIRS) onboard S-NPP over Greenland (left), where one of the SNO between S-NPP and METOP-B occurred. The image on the right shows the size, shape, and orientation of OMPS and GOME-2 instantaneous field of view, as well as the scene homogeneity for this SNO event.

The premise of inter-comparing satellite instruments is the assumption that measurements should be the same if they were made at the same time, with the same viewing geometry, of the same target, and over the same spectral range. In practice, measurements can be inter-compared only after carefully considering and properly accounting for discrepancies in each of those categories [*Wu et al.*, 2009; *Hewison et al.*, 2013].

2.1. Temporally Concurrent

The differences in observation times are less than 2 min in all SNO events (often much less). It is assumed that changes in illumination and atmospheric status within that short period of time are insignificant to cause systematic differences in measurements.

2.2. Geometrically Aligned

The OMPS TC SDR generated by the IDPS has a nadir "macropixel." The level 1b data product of GOME-2, on the other hand, has two "subsets" (13 and 14) adjacent to the nadir. This means that the viewing geometry cannot be identical for OMPS and GOME-2 during SNO; however, since they are very close to nadir, these differences are also neglected.

2.3. Spatially Collocated

The field of view (FOV) at nadir is 40 km by 80 km (along- and cross-track) for GOME-2 (Band 2) and 50 km by 50 km for OMPS. They are not identical in size, shape, and orientation and therefore cannot be overlapped perfectly. Figure 2 is an example, where the overlap between the two FOVs is typical among the SNO events examined. No attempt was made to reconcile these differences. In general, these differences may cause random differences in measurements, but not systematic difference. In particular, if the scene is uniform, such as shown in Figure 2, spatial mismatch should cause little difference in measurements. Note that the absence of clouds, or the appearance of uniformity in some visible spectrum, is not always critical for evaluating some OMPS channels. Because of the spectral absorption of ozone and the fact that most ozone is above clouds, channels that are nearly opaque to ozone are less affected by cloud reflection. Thus, to the extent that the horizontal distribution of ozone is more uniform than that of clouds, which is often the case, regions that are not uniform in visible and some OMPS channels could still be reasonably uniform for other OMPS channels that are so strongly subject to ozone absorption that mismatch in space would cause little discrepancy. This does not apply to the relatively rare cases where the horizontal distribution of ozone is not uniform, which can happen in polar regions.

2.4. Spectrally Consistent

The spectral resolution is 1.0 nm for OMPS and 0.27 nm for GOME-2, and the sampling interval is 0.41 nm for OMPS and 0.12 nm for GOME-2. To reconcile these differences, GOME-2 data are considered as

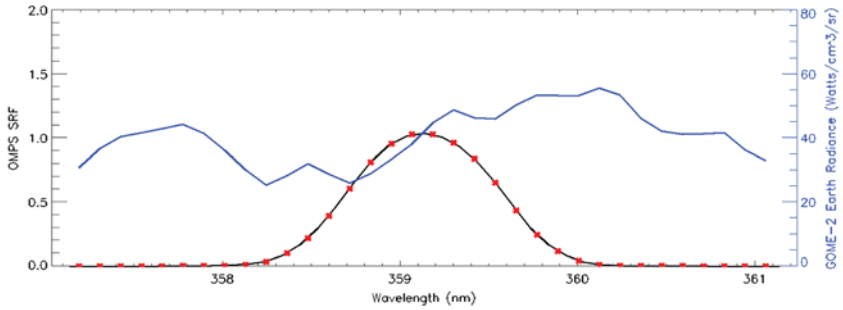

Figure 3. Spectral response function (SRF) of an OMPS channel (black, left coordinate), over plotted with a GOME-2 spectral radiance (blue, right coordinate). The red dots are where the OMPS SRF is specified at and the GOME-2 measurements are interpolated to.

monochromatic measurements at the channel center wavelength and convoluted with the OMPS spectral response function (SRF):

$$m^j = \frac{\sum_{i=1}^{n} m_i \Phi_i^j}{\sum_{i=1}^{n} \Phi_i^j} \tag{1}$$

where j is the OMPS channel index, for NM $j = [1,196]$; m^j is the convoluted GOME-2 measurements for OMPS Channel j that can be earth radiance R, solar irradiance I, or reflectance ρ; m_i is the GOME-2 measurement at wavelength i; Φ_i^j is the OMPS SRF for channel j interpolated to wavelength i; and n is the number of wavelength for which OMPS NM SRF is specified (nominally $n = 41$). Reflectance ρ is computed as:

$$\rho = \frac{\pi R}{I \cos\theta_0} \tag{2}$$

where θ_0 is the solar zenith angle. In (1) and (2), spectral dependence of ρ, R, and I is understood but omitted for brevity. The I in (2) is the instantaneous solar irradiance, which can be approximated by GOME-2 daily measurement of solar irradiance. For OMPS, one must account for the variation of the Sun-Earth distance when using the solar irradiance at the unit astronomical unit that OMPS reports. Figure 3 is an example of OMPS SRF and GOME-2 spectral measurements (earth radiance in this case).

Results of the two SNO comparisons are summarized in Figure 4. In the solar irradiance comparison with METOP-A (panel a), OMPS measurements are more than two times larger than GOME-2 measurements, increasing with decreasing wavelength. Similarly, OMPS earth radiance (panel c) is also two times larger than GOME-2 but nearly flat spectrally. Finally, reflectances from OMPS and METOP-A GOME-2 (panel e) follow each other closely and the ratio is closer to unity. These results confirmed the independent conclusions [*Lang*, 2012] that, after more than 6 years in orbit, the signal throughputs of GOME-2 on METOP-A have decreased for both the earthshine and solar measurements by up to 50%. However, the ratios between the two, the reflectances (panel e) that are the primary products of GOME-2, are much less affected by the degradation, especially for channels at longer wavelength. Furthermore, since the plot in (c) shows only the GOME-2 instrument (sensor and optics) degradation whereas the plot in (a) includes additional solar diffuser degradation, these comparisons demonstrated that the GOME-2 solar diffuser has degraded more at shortwave than at longwave. This spectrally differential degradation, a commonly observed trend, led to the current 10–15% discrepancy in reflectances for the shortwave channels, which has also been observed by the GOME-2 team [*Lang*, 2013].

Figure 4 also showed that the GOME-2 on METOP-B compared much better with OMPS, both in terms of solar irradiance (panel b) and earth radiance (panel d), and especially in terms of reflectances (panel e) that are within 1% for most channels. This consistency is in part because both instruments were relatively new in orbit, and is encouraging evidence that the pre-flight characterization and the transition of ground to flight calibration for both instruments were successful. On the other hand, the METOP-B GOME-2 reflectance is a little higher for the shortwave channels than for the longwave channels, a trend that is opposite to that of METOP-A GOME-2 at present and should be understood and monitored in future.

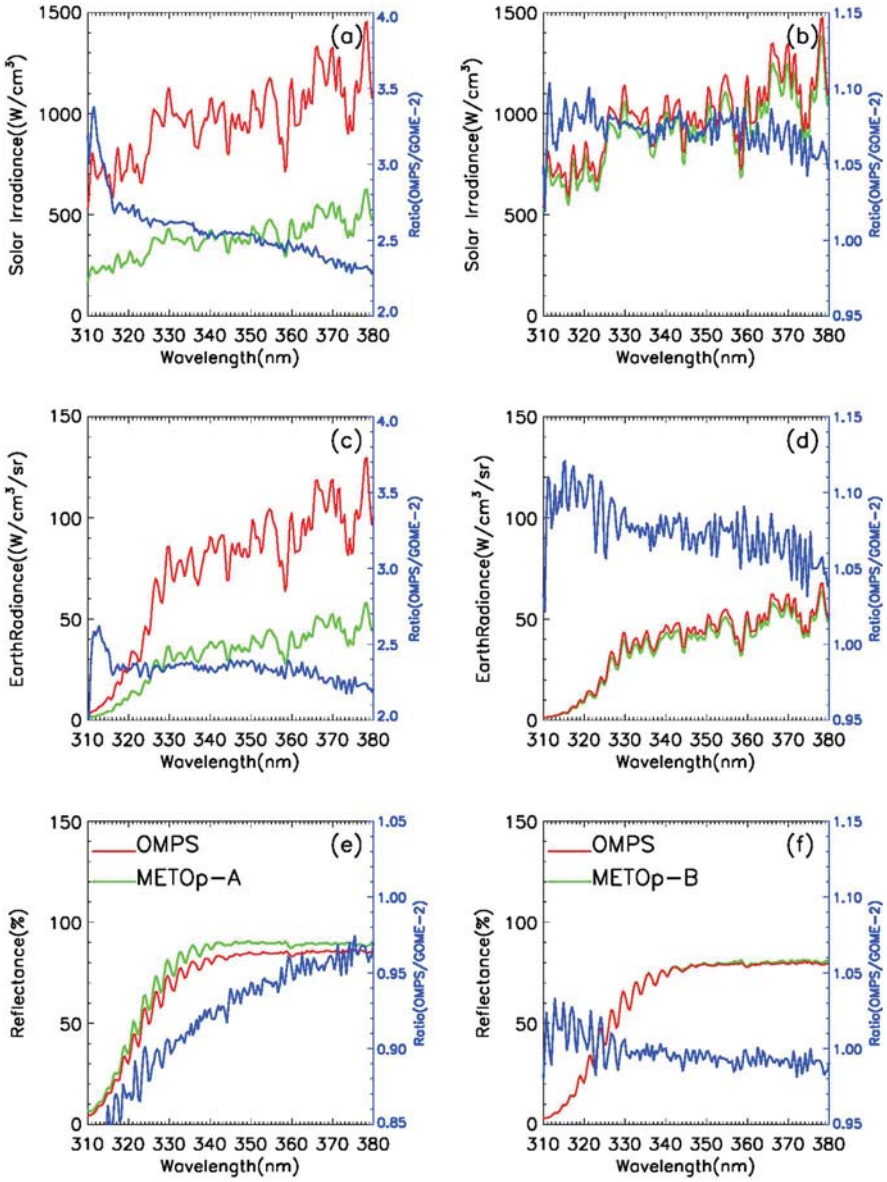

Figure 4. SNO comparison of solar irradiance (upper row), Earth radiance (middle row), and reflectance (lower row) between OMPS measurement (red) and GOME-2 measurement (green) on (left column) METOP-A and (right column) METOP-B. Also shown in each plot, in blue and using the ordinate to the right, is the ratio of OMPS measurement to the convoluted GOME-2 measurement.

Figure 5 are time series of the reflectance ratio of OMPS to METOP-A (left panel, eight ratios) and METOP-B (right panel, five ratios) for selected wavelengths. Each ratio is the average of 10–30 SNO events similar to the one analyzed in Figure 4 that typically occur during a period of 1–3 days (see Figure 1 for SNO events in 1 day). Relative to METOP-B GOME-2, METOP-A GOME-2 appears to differ more from OMPS but has also been more stable during the period of comparison. These are consistent with the fact that, at the time of comparison, METOP-A/B GOME-2 are about 7 years and 7 months in orbit, respectively. Instrument degradation tends to be faster when initially deployed in orbit (GOME-2 on METOP-B) and becomes stabilized after a few years (GOME-2 on METOP-A). Within each instrument, there appear more changes for shorter wavelength channels than for longer wavelength channels, which is particularly evident for METOP-B GOME-2. While none of these findings are unexpected, they are preliminary in nature, and conclusions must wait for further collection and analysis of SNO comparisons in future.

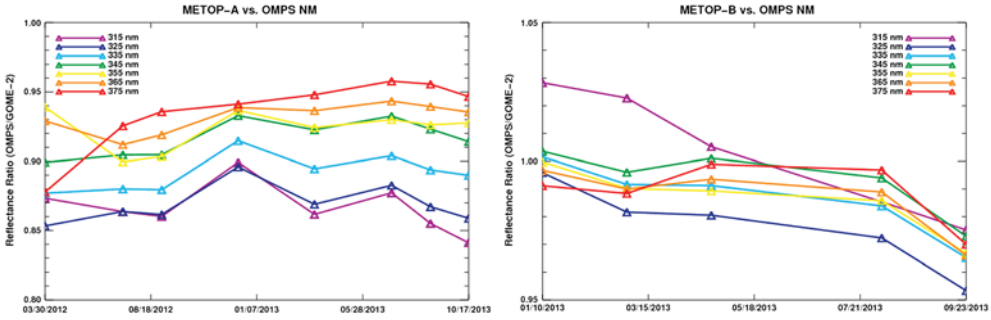

Figure 5. Time series of SNO comparisons between OMPS and GOME-2 on (left) METOP-A and (right) METOP-B for selected wavelengths.

It is also possible to compare OMPS NP (spectral coverage 250–310 nm) with Band 1A (240–283 nm) and 1B (283–311 nm) of GOME-2 (these are the valid spectral range). Results from cursory comparisons of OMPS NP with METOP-B GOME-2 for solar irradiance (not shown) are broadly in agreement with similar comparisons for NM. The difficulty of extending these comparisons for earth view measurements arises from the differences in spatial resolution between these two sensors. OMPS NP has one field of view of 250 km by 250 km at nadir. The footprint of GOME-2 Band 1A is usually 40 km by 640 km, making it impossible to have more than 40% of overlapping region between the two sensors. The footprint of Band 1B is 40 km by 80 km in forward scan and 40 km by up to 240 km in backward scan. While possible, it is more difficult to spatially colocate the two sensors, even more difficult to automate the process due to varying operation mode of GOME-2 Band 1. However, work is underway to take advantage of the fact that all OMPS NP channels are subject to strong absorption by ozone, which usually is uniformly distributed at the spatial scale of interest and largely above clouds such that even measurements that are severely mismatched in space can yield meaningful results. NM measurements can be used to screen out the SNO events that occur where the horizontal gradient of ozone distribution is of concern.

3. Comparison With CRTM

The Community Radiative Transfer Model [CRTM, *Han et al*., 2006] was developed at the Joint Center for Satellite Data Assimilation, primarily in support for the operational satellite radiance assimilation for numerical weather prediction models. However, as previously demonstrated [*Wang et al*., 2011; *Rama Varma Raja et al*., 2012; *Chen et al*., 2013], it is also a powerful tool in evaluating satellite instrument performance. The four modules of the CRTM are gaseous transmittance, surface emission and reflection, cloud and aerosol absorption and scatterings, and solver for radiative transfer. The gaseous transmittance describes the interactions (absorption and scattering) of various atmospheric gases [H_2O, CO_2, O_3, N_2O, CO, CH_4, and others, see *Chen et al*., 2012] with radiation in a wide range of spectrum, from ultraviolet to microwave. This enables the detection of the distribution of these gases and their physical environment (temperature, pressure) using remotely sensed data. The aerosol and cloud module describes the interactions of other atmospheric constituents with radiation to enable the investigations of those constituents. The surface module provides additional constraints and options to simulate the radiative transfer process. Two radiative solvers have been implemented into the CRTM, the advanced doubling-adding method [*Liu and Weng*, 2006] as the baseline and the successive order of interaction [*Heidinger et al*., 2006] as an alternative.

While the current CRTM does not include the OMPS sensor, it has the flexibility to incorporate other gaseous modules. Several radiative transfer models designed for the ultraviolet spectrum are available, including those for TOMS [TOMRAD, *Eck et al*., 1995], for GOME [GOMETRAN, *Rozanov et al*., 1997] and later for SCHIAMACHY [SCIATRAN, *Rozanov et al*., 2005], the Linearized Discrete Ordinate Radiative Transfer [LIDORT, *Spurr et al*., 2001] and its vectorized version [VLIDORT, *Spurr*, 2006], and the Library for Radiative Transfer [libRadTran, *Arola et al*., 2005]. The libRadTran was used in this study, in conjunction with the CRTM, to simulate the spectral radiance at the top of the atmosphere (TOA) that would be observed by OMPS nadir sensors. Input parameters include the vertical distribution of temperature and moisture, and ozone below 200 hPa, from the European Center for Medium-range Weather Forecast 6 h forecast interpolated to the location in question; ozone profile above 200 hPa from OMPS NP products; geometric parameters such as the

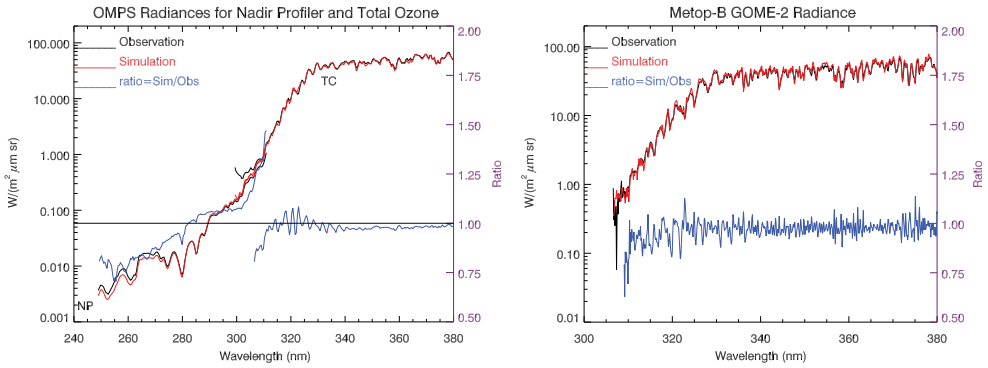

Figure 6. Measured (black) and simulated (red) radiances and the ratio of the two (green, simulated/measured) for (left) S-NPP OMPS and for (right) METOP-B GOME-2.

zenith and azimuth angles of OMPS and the Sun; and the spectral response functions for OMPS and GOME-2. The atmosphere is assumed to be free of cloud and aerosol. The surface albedo is set to a constant of 0.97 for the homogeneous snow-covered Greenland (Figure 2). Effects of surface bidirectional reflectance distribution function are not considered, because the polarized version of the radiative transfer model accepts the Lambertian surface only. The solar irradiance by *Chance and Kurucz* [2010] at a spectral resolution of 0.01 nm is used. Radiative transfer models in the UV spectrum simulate the process of solar radiation entering the TOA from certain direction, interacting (absorption and/or scattering) with atmospheric constituents (and the underlying surface if relevant), and eventually emerging the TOA toward the sensor. Results of such simulation depend in part on the characteristics of the incoming solar radiation. For that reason, the simulated radiance is further scaled by the OMPS measured solar irradiance to minimize the difference due to the TOA solar irradiance:

$$R^j_{\text{scaled}} = R^j_{\text{simulated}} \frac{I^j_{\text{measured}}}{\int I(\lambda)\Phi(\lambda)^j d\lambda} \tag{3}$$

where j is the OMPS channel index (unitless); R_{scaled} and $R_{\text{simulated}}$ are, respectively, the scaled and simulated earth view radiance in mW m^{-2} nm^{-1} str^{-1}; I_{measured} and $I(\lambda)$ are, respectively, the measured and reference [*Chance and Kurucz*, 2010] solar irradiance in mW m^{-2} nm^{-1}; and $\Phi(\lambda)$ is the OMPS spectral response function (unitless). The integration is over the spectral range where $\Phi(\lambda)^j$ is specified [*Hornstein et al.*, 2002].

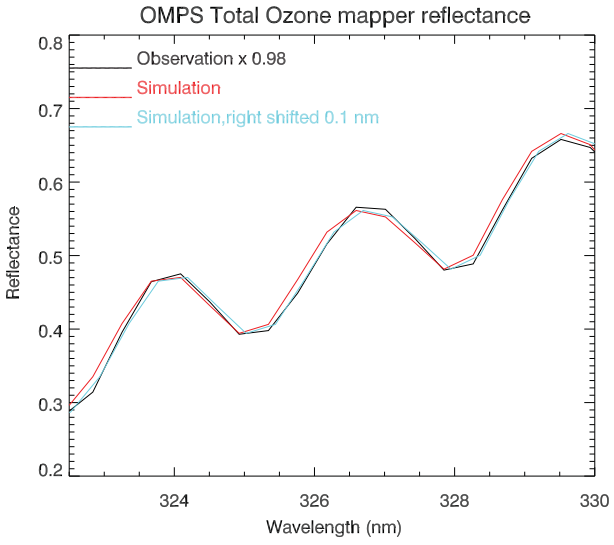

Figure 7. Measured (black), simulated (red), and shifted (cyan) OMPS NM radiance.

Results of comparisons are shown in Figure 6. For OMPS (left panel), the simulations generally agree with the measurements, especially for NM. The discrepancy with NP is larger in general and also varies spectrally for wavelength shorter than approximately 285 nm. The ratio of the two radiances (simulated over measured) shows increasing discrepancy in the overlapping region (300–310 nm). Radiance entering the OMPS aperture is separated by a dichroic beam splitter that reflects the shortwave radiance to NP and transmits the longwave radiance to NM. It is believed that uncertainty in the dichroic spectral characteristics is largely responsible for the discrepancy for NP. For NM, there is an additional effect of stray

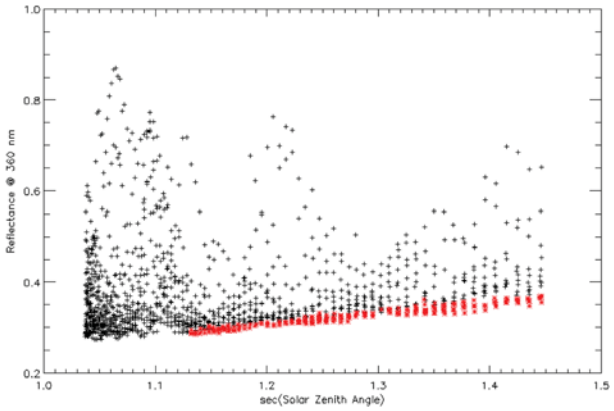

Figure 8. Apparent reflectances at 360 nm for pixels at the cross track position 2, collected over the Tropical Pacific (20°S–20°N, 100°W–180°W) during a week in June 2012 and plotted as a function of $sec(\theta_0)$, the secant of the solar zenith angle of the pixel.

light that has not been corrected for the data used. The right panel of Figure 6 is the similar comparison for METOP-B GOME-2. It shows an excellent agreement between the measured and simulated radiances for wavelength longer than 315 nm, where the Band 2B data are considered valid. The solar irradiance was also scaled with GOME-2 observed irradiance similar to (3).

Closer inspection of Figure 6 suggests that the measured and simulated radiances around 320 nm appear out of phase, which may also be partially responsible for the oscillation in the ratio in that spectral region. To quantify, correlation coefficient r is computed for a range of wavelength shift $\Delta\lambda$ in increment of 0.01 nm:

$$r(\Delta\lambda) = Corr\_Coeff\left[R^{j}_{measured}, \int R(\lambda+\Delta\lambda)\Phi^{j}(\lambda)d\lambda\right] \quad (4)$$

where j is the index of OMPS channel between 220 and 230 nm. The correlation r reaches its maximum when $\Delta\lambda = +0.1$ nm. As shown in Figure 7, the simulated radiance with the optimal wavelength shift agrees better with the measured radiance. However, the suggested shift is preliminary, as the magnitude of the shift (+0.1 nm) is larger than the findings by some researchers (e. g., C. Seftor, and L. Flynn, personal communications). Note that the OMPS measured solar irradiance is used in simulation to scale the solar irradiance used in RTM; therefore, uncertainty in that measurement affects the earth view simulation as well.

4. Product Stability

Tracking radiance from stable earth targets has long been used to evaluate the stability of satellite instrument performance, especially for those sensing the reflected (or scattered) solar radiation. While necessary for vicarious calibration of earlier sensors that have no onboard calibration devices [*Wu et al*., 2010], the technique also proves useful for sensor with sophisticated onboard calibration [*Sun et al*., 2012].

Radiance sensed by OMPS over clear ocean is dominated by molecular scattering, subject to interactions with ozone and aerosols. In the absence of major event such as Mt. Pinatubo eruption, aerosol concentration is relatively low over the Tropical Pacific (20°S–20°N, 100°W–180°W), in particular the variation of aerosol concentration in time and space is small in the region. Rayleigh scattering depends on molecular concentrations, which are nearly invariant in the region; on viewing zenith angle θ, which is constant for a cross track position; and on solar zenith angle θ_0, which is known accurately. Thus, clear ocean radiance over the Tropic Pacific can be regarded as stable and used to assess OMPS SDR stability at selected wavelengths.

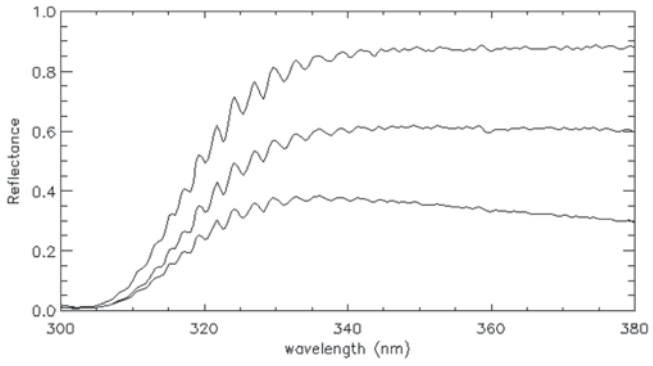

Figure 9. OMPS spectral reflectance over regions of (lower) clear ocean, (middle) cloudy ocean, and (upper) deep convective cloud.

Care should be taken in identifying clear ocean radiance. One common practice is to choose the darkest pixel over a region and a period of time, assuming that higher reflectance reveals the presence of clouds. Since clear pixels are presumably abundant in this region, even at the OMPS spatial resolution, it is sensible to use the darkest 1% instead of the darkest to reduce the variation of extreme values. *Flynn et al*. [2014], for

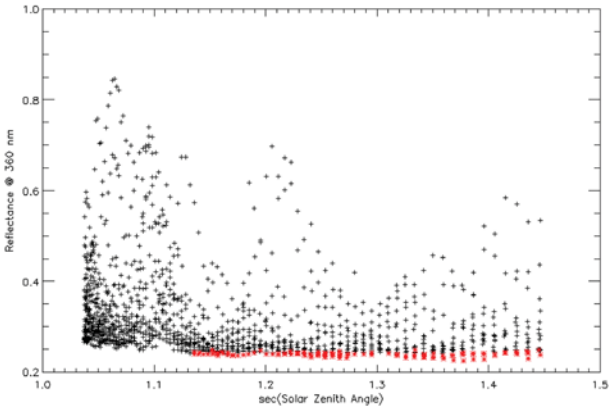

Figure 10. As Figure 8, but for the adjusted reflectance that accounts for the enhanced Rayleigh scattering with increased path length or $sec(\theta_0)$.

example, used the darkest 1% of the retrieved reflectances for selected channels to evaluate product stability. However, if the target of monitoring is an SDR such as radiance or apparent reflectance, it should be realized that the clear pixels may not have the minimal values. As illustrated in Figure 8, criteria based on the apparent reflectance would lead to the implausible conclusion that pixels with larger solar zenith angle, such as those marked in red, could never be considered clear. This is because Rayleigh scattering increases with path length that is proportional to $sec(\theta_0)$; therefore, enhanced Rayleigh scattering at larger solar zenith angle makes those pixels to appear brighter than if viewed at smaller solar zenith angle. Another consequence is that slightly contaminated pixels with smaller solar zenith angle may appear darker than clear pixels with larger solar zenith angle. For both reasons, apparent reflectance is not suitable to determine clear pixel.

It is possible, on the other hand, to take advantage of the hyperspectral nature of the OMPS data to identify clear pixels by their spectral characteristics. Figure 9 shows three spectral reflectances over clear ocean, cloudy ocean, and deep convective clouds (DCC) in the Tropical Pacific. Note that not only the mean reflectance is progressively higher for increasing cloudiness; their spectral characteristics are also different. Over clear ocean, reflectance at 380 nm is slightly lower than, say, at 340 nm, because Rayleigh scattering is stronger for shorter wavelength. With DCC acting as a proxy of Lambertian diffuser near the TOA and Rayleigh scattering no longer dominates, the spectral difference of reflectances is reduced or even reversed such that the reflectance at 380 nm can be slightly higher than at 340 nm for DCC, due in part to the increasing solar irradiance at longer wavelength. The spectral dependence of the cloudy pixel is somewhere between these two cases. This suggests that $dR/d\lambda$, the derivative of reflectance with respect to wavelength in the spectral range of 340 nm to 380 nm, can be exploited as a tool to infer how clear a pixel is.

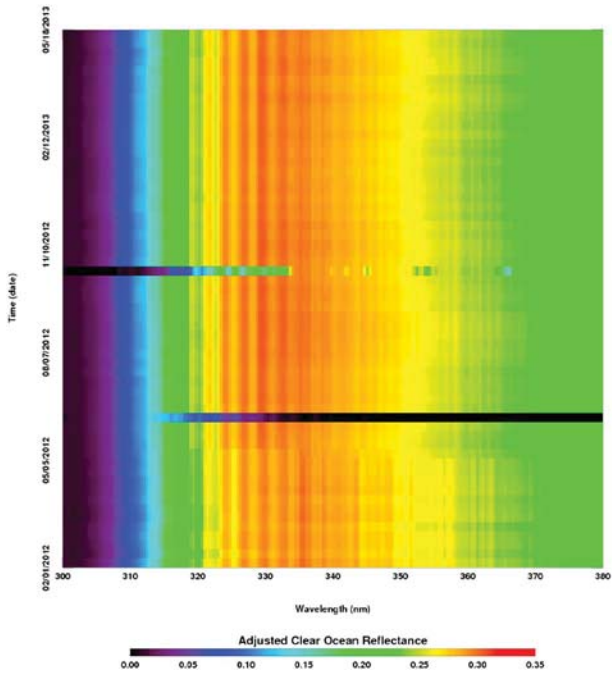

Figure 11. Darkest 1% adjusted reflectance at cross track position 21, for the 196 channels of OMPS NM in the first 70 weeks of operation.

Clear pixels identified by $dR/d\lambda$ are marked in Figure 8 as red, which no longer exclude pixels with larger solar zenith angle. Furthermore, the dependence of clear pixel reflectance on $sec(\theta_0)$ can be quantified to account for the variation of Rayleigh scattering with $sec(\theta_0)$. Figure 10 is a similar plot as Figure 8, with the apparent reflectance adjusted to $sec(\theta_0) = 1$. The adjusted reflectance provides a leveled ground to identify clear pixels.

The darkest 1% of the adjusted OMPS NM reflectances at the cross track position 21 is shown in Figure 11 for the 196 channels of NM and for the first 15 months of OMPS operation. Along the horizontal direction in this chart is the spectral variation of clear ocean reflectance in a week. Familiar features for all weeks (except for the two known anomalies in June and October 2012)

include the low reflectance below 305 nm due to broad and strong ozone absorption, the rapid increase of reflectance towards 315 nm, the reflectance plateau with oscillation up to 350 nm due to spectrally selective ozone absorption, and the gradual decrease towards 380 nm with some Fraunhofer lines still discernible. On the other hand, along the vertical direction is the variation (or the lack thereof) over time for each channel. For example, the changes around 311 nm indicate temporal variation of reflectance measurements for those channels, which are likely caused by genuine ozone variation in time. A small but noticeable increase across all channels is found in May 2012, corresponding to the update of Day 1 solar irradiance at the time. There are more subtle variations; the reasons for all these are the subject of further investigations. Overall, however, the OMPS NM SDR from IDPS appear reasonably stable.

5. Summary and Conclusions

This paper provided a preliminary evaluation of the OMPS SDR from IDPS, using the first 15 months of data. While not a comprehensive and detailed validation, this evaluation gave an initial assessment of the overall data quality. Based on comparisons with the data from GOME-2 on METOP-A/B and with the simulations by the CRTM, and an assessment of stability, this evaluation found no gross error or unexpected characteristics in the OMPS nadir SDR produced by the IDPS. The data quality is satisfactory for the current Provisional maturity.

This evaluation is part of the OMPS post-launch calibration and validation activities that also include the evaluation of sensor calibration and EDR products performance, for example *Pan et al*. [2013], and other papers in the Special Issue. The goal is to provide a comprehensive assessment, or multiple assessments if possible, for every link of the product chain to ensure the quality. Evaluation of OMPS nadir SDR from IDPS will continue and expand, including refinement of existing and development of new validation methods and in-depth analysis of validation results. As demonstrated in this study, international collaboration is very important in this effort, to that extent a working subgroup is being established within the Global Space-based Inter-Calibration System [GSICS, *Goldberg et al*., 2011]. The goal is to assess the product quality at the Validated maturity and to ensure the product quality during the LTM phase of the S-NPP mission.

Acknowledgments

This work was supported by the NOAA JPSS and NASA S-NPP programs. The authors are grateful to R. Lang and R. Munro for valuable discussions about GOME-2, to NOAA Calibration Center for help with SNO, and to three reviewers of an earlier draft of this paper that substantially improved the paper. The contents of this manuscript are solely the opinions of the authors and do not constitute a statement of policy, decision, or position on behalf of NOAA or the U.S. Government.

References

Arola, A., S. Kazadzis, N. Krotkov, A. Bais, J. Gröbner, and J. R. Herman (2005), Assessment of TOMS UV bias due to absorbing aerosols, *J. Geophys. Res.*, *110*, D23211, doi:10.1029/2005JD005913.

Cao, C., M. Weinreb, and H. Xu (2004), Predicting simultaneous nadir overpasses among polar-orbiting meteorological satellites for the intersatellite calibration of radiometers, *J. Atmos. Oceanic Technol.*, *21*, 537–542, doi:10.1175/1520-0426(2004)021<0537:PSNOAP>2.0.CO;2.

Chance, K., and R. L. Kurucz (2010), An improved high-resolution solar reference spectrum for Earth's atmosphere measurements in the ultraviolet, visible, and near infrared, *J. Quant. Spectros. Radiat. Transfer*, *111*, 1289–1295.

Chen, Y., Y. Han, and F. Weng (2012), Comparison of two transmittance algorithms in the community radiative transfer model: Application to AVHRR. *J. Geophys. Res.*, *117*, D06206, doi:10.1029/2011JD016656.

Chen, Y., Y. Han, P. van Delst, and F. Weng (2013), Assessment of Shortwave Infrared Sea Surface Reflection and Nonlocal Thermodynamic Equilibrium Effects in the Community Radiative Transfer Model Using IASI Data, *J. Atmos. Oceanic Technol.*, *30*, 2152–2160, doi:10.1175/JTECH-D-12-00267.1.

Eck, T. F., P. K. Bhartia, and J. B. Kerr (1995), Satellite Estimation of spectral UVB irradiance using TOMS derived ozone and reflectivity, *Geophys. Res. Lett.*, *22*, 611–614.

Flynn, L., C. Seftor, J. Larsen, and P. Xu (2006), Introduction to the Ozone Mapping and Profiler Suite (OMPS), in *Earth Science Satellite Remote Sensing Vol.1: Science and Instruments*, edited by J. J. Qu et al., Springer, Berlin, ISBN: 978-3-540-35606-6. Also http://npp.gsfc.nasa.gov/omps.html.

Flynn, L., et al. (2014), Performance of the ozone mapping and profiler suite (OMPS) products, *J. Geophys. Res. Atmos.*, doi:10.1002/2013JD020467.

Goldberg, M., et al. (2011), The global space-based inter-calibration system, *Bull. Am. Meteorol. Soc.*, *92*(4), 467–475.

Gottwald, M., et al. (2006), SCIAMACHY, Monitoring the Changing Earth's Atmosphere; Published by DLR. [Available at http://atmos.caf.dlr.de/projects/scops/sciamachy_book/sciamachy_book.html.]

Han, Y., P. van Delst, Q. Liu, F. Weng, B. Yan, R. Treadon, and J. Derber (2006), Community Radiative Transfer Model (CRTM) — Version 1, *NOAA NESDIS Tech. Rep. 122*, 22 pp., Natl. Oceanic and Atmos. Admin., Silver Spring, Md.

Heidinger, A. K., O. Christopher, R. Bennartz, and T. Greenwald (2006), The Successive-Order-of-Interaction Radiative Transfer Model. Part I: Model Development, *J. Appl. Meteorol.*, *45*, 1388–1402.

Hewison, T. J., X. Wu, F. Yu, Y. Tahara, X. Hu, D. Kim, and M. Koenig (2013), GSICS Inter-Calibration of Infrared Channels of Geostationary Imagers Using Metop/IASI, *IEEE Trans. Geosci. Remote Sens.*, *51*(3), 1160–1170, doi:10.1109/TGRS.2013.2238544.

Hilsenrath, E., R. P. Cebula, M. T. Deland, K. Laamann, S. Taylor, C. Wellemeyer, and P. K. Bhartia (1995), Calibration of the NOAA 11 solar backscatter ultraviolet (SBUV/2) ozone data set from 1989 to 1993 using in-flight calibration data and SSBUV, *J. Geophys. Res.*, *100*, 1351–1366.

Hornstein, J., E. P. Shettle, R. M. Bevilacqua, S. Chang, E. Colon, L. Flynn, E. Hilsenrath, S. Mango, H. Bloom, and F. Sanner (2002), The Ozone Mapping and Profiler Suite-Assimilation Experiment (OMPS-AE), *Int. Geosci. Remote Sens. Symp.*, *2*, 809–812.

Jaross, G., P. K. Bhartia, G. Chen, M. Kowitt, M. Haken, Z. Chen, P. Xu, J. Warner, and T. Kelly (2014), OMPS Limb Profiler instrument performance assessment, *J. Geophys. Res. Atmos.*, *119*, 4399–4412, doi:10.1002/2013JD020482.

Klaes, K. D., et al. (2007), An Introduction to the EUMETSAT Polar system, *Bull. Am. Meteorol. Soc.*, *88*, 1085–1096, doi:10.1175/BAMS-88-7-1085.

Lang, R. (2012), GOME-2 / Metop-A Level 1B Product Validation Report No. 5: Status at Reprocessing G2RP-R2v1F, Report EUM/OPS-EPS/REP/09/0619, EUMETSAT.

Lang, R. (2013), EPS Metop-B Product Validation Report: GOME-2 Level 1, EUM/OPS-EPS/DOC/12/0760. [Available at http://www.eumetsat.int/website/wcm/idc/idcplg?IdcService=GET_FILE&dDocName=pdf_gome_l1_mb_prod_val&RevisionSelectionMethod=LatestReleased&Rendition=Web.]

Levelt, P. F., E. Hilsenrath, G. W. Leppelmeier, G. H. J. van den Oord, P. K. Bhartia, J. Tamminen, J. F. de Haan, and J. P. Veefkind (2006), Science objectives of the ozone monitoring instrument, *IEEE Trans. Geosci. Remote Sens.*, *44*(5), 1199-1208, doi:10.1109/TGRS.2006.872336. [Available at http://aura.gsfc.nasa.gov/instruments/omi.html.]

Liu, Q., and F. Weng (2006), Advanced doubling-adding method for radiative transfer in planetary atmosphere, *J. Atmos. Sci.*, *63*, 3459–3465.

McPeters, R. D., et al. (1996), *Nimbus-7 TOMS Ozone Mapping Spectrometer (TOMS) Data Products User's Guide*, NASA Reference Publication, vol. 1384, National Aeronautics and Space Administration, Washington, D. C. [Available at http://macuv.gsfc.nasa.gov/doc/n7usrguide.pdf.]

Munro, R., R. Lang, Y. Livschitz, J. Kujanpää, D. Loyola, P. Valks, P. Stammes, and O. Tuinder (2008), GOME-2 mission and product validation status. EUMETSAT User Conference, Darmstadt, Germany, 8-12 Sept.

Pan, C., M. Kowalewski, R. Buss, L. Flynn, X. Wu, M. Caponi, and F. Weng (2013), Performance and calibration of the nadir Suomi-NPP Ozone Mapping Profiler Suite from early-orbit Images, *IEEE J. Sel. Top. Appl. Earth Obs. Remote Sens.*, *6*(3), 1539–1551, doi:10.1109/JSTARS.2013.2259144.

Rama Varma Raja, M. K., X. Wu, and F. Yu (2012), Assessment of MetOp-A Advanced Very High Resolution Radiometer (AVHRR) short-wave infrared channel measurements using Infrared Atmospheric Sounding Interferometer (IASI) observations and line-by-line radiative transfer model simulations, *Int. J. Remote Sens.*, *33*(16), 5240–5250.

Rodriguez, J. V., C. J. Seftor, C. G. Wellemeyer, and K. Chance (2003), An overview of the nadir sensor and algorithms for the NPOESS ozone mapping and profiler suite (OMPS), *Proc. SPIE*, 4891, doi:10.1117/12.467525.

Rozanov, V. V., D. Diebel, R. J. D. Spurr, and J. P. Burrows (1997), GOMETRAN: A radiative transfer model for the satellite project GOME – the plane-parallel version, *J. Geophys. Res.*, *102*(D14), 16,683–16,695.

Rozanov, A., V. Rozanov, M. Buchwitz, A. Kokhanovsky, and J. P. Burrows (2005), SCIATRAN 2.0 – A New Radiative Transfer Model for Geophysical Applications in the 175 – 2400 nm spectral region, *Adv. Space Res.*, *36*, 1015–1019.

Spurr, R. J. D. (2006), VLIDORT: A linearized pseudo-spherical vector discrete ordinate radiative transfer code for forward model and retrieval studies in multilayer multiple scattering media, *J. Quant. Spectrosc. Radiat. Transfer*, *102*, 316–342, doi:10.1016/j/jqsrt.2006.05.005.

Spurr, R., T. Kurosu, and K. Chance (2001), A linearized discrete ordinate radiative transfer model for atmospheric remote sensing retrieval, *J. Quant. Spectrosc. Radiat. Transfer*, *68*, 689–735.

Sun, J., A. Angal, X. J. Xiong, H. Chen, X. Geng, A. Wu, T. Choi, and M. Chu (2012), MODIS RSB calibration improvements in Collection 6, *Proc. SPIE*, 8528, doi:10.1117/12.979733.

Wang, L., C. Zou, and H. Qian (2011), Construction of stratospheric temperature data records from Stratospheric Sounding Units (SSU), *J. Clim.*, *25*, 2931–2946.

Wu, X., T. Hewison, and Y. Tahara (2009), GSICS GEO-LEO inter-calibration: Baseline algorithm and early results, *Proc. SPIE*, *7456*, 745604-1–745604-12.

Wu, X., J. T. Sullivan, and A. K. Heidinger (2010), Operational calibration of the Advanced Very High Resolution Radiometer (AVHRR) visible and near-infrared channels, *Can. J. Remote Sens.*, *36*(5), 602–616, doi:10.5589/m10-080.